Analysis and Design of a CMOS Angular Velocity- and Direction-Selective Rotation Sensor With a Retinal Processing Circuit

Kuan-Hsun Huang, *Member, IEEE*, Li-Ju Lin, *Student Member, IEEE*, and Chung-Yu Wu, *Fellow, IEEE*

Abstract—This paper implements and analyzes a CMOS angular velocity- and direction-selective rotation sensor with a retinal processing circuit. The proposed rotation sensor has a polar structure and is selective of the angular velocity and direction (clockwise and counterclockwise) of the rotation of images. The correlation-based algorithm is adopted and each pixel in the rotation sensor is correlated with the pixel that is 45° apart. The angular velocity selectivity is enhanced by placing more than one pixel between two correlated pixels. The angular velocity selectivity is related to both the number and the positions of the edges in an image. Detailed analysis characterizes angular velocity selectivity for different edges. An experimental chip consisting 104 pixels, which form five concentric circles, is fabricated. The single pixel has an area of $91 \times 84 \, \mu\text{m}^2$ and a fill factor of 20%, whereas the area of the chip is $1812 \times 1825 \, \mu\text{m}^2$. The experimental results concerning the fabricated chip successfully verified the analyzed characteristics of angular velocity and direction selectivity. They showed that the detectable angular velocity and range of illumination of this rotation sensor are from $2.5 \times 10^{-3} \, \pi/\text{s}$ to $40 \, \pi/\text{s}$ and from 0.91 lux to 366 lux, respectively.

Index Terms—Focal-plane motion sensor, motion sensor, retinal processing circuit, rotation sensor, vision chip.

I. INTRODUCTION

MOTION provides rich cues in understanding the environment and is, therefore, crucial for many applications including robot control, vehicle navigation, and surveillance systems. Recently, much research effort has been devoted to focal-plane motion sensors, which integrate photo sensing and signal processing into a single chip [1]. Focal-plane motion sensors are superior in size, processing time, cost, and power consumption than conventional image processing systems, which include cameras and processors. Many focal-plane motion sensors adopt the correlation-based algorithm to detect motion [2]–[8]. The correlation-based algorithm, inspired by a biological model [9], provides the advantages of robustness and compactness and is, thus, the most practical algorithm for focal-plane motion sensor.

In previously proposed focal-plane motion sensors, the spatial distribution of the pixels is typically regular and periodic because these sensors are intended to detect invariants in Cartesian coordinates. For these sensors, a mapping from Cartesian to polar coordinates is required to detect rotation. However, if the pixels are placed in a polar arrangement, rotation can be detected by shifting the images in the θ direction so complex mapping can be avoided.

The correlation-based algorithm is adopted by the proposed rotation sensor to detect the local motion vectors, whereas the retinal processing circuit [8], [10], [11], which mimics some of the functions of the cells in the outer plexiform layer of the real retina, is used to sense and preprocess the incident images. The output of the retinal processing circuit can adapt to the background illumination so that a high optical dynamic range can be obtained. The pixels of the proposed rotation sensor are placed in a circular arrangement to detect the global rotation direction and velocity of the rotating images. There are totally 104 pixels, which form five concentric circles. The numbers of pixels in the circles are 8, 16, 16, 32, and 32 in order from the center. Every pixel is correlated with clockwise and counterclockwise pixels that are 45° apart. Local motion vectors are detected by the correlators in each pixel. The outputs of all correlators in a single circle are aggregated to determine the velocity and direction of the global rotation. The proposed rotation sensor is selective to the angular direction and velocity of rotating images. The selected angular velocity is controlled by the frequency of an external clock signal. The angular velocity selectivity is enhanced by placing more than one pixel between two correlated pixels and correlating with the pixel that is 45° apart. The angular velocity selectivity is analyzed and equations are derived to describe the angular velocity selectivity. If the incident image has multiple edges, then the angular velocity selectivity is related to both the number and the positions of the edges and the angular velocity selectivity is expressed by a set of inequalities.

The advantageous characteristics of the proposed rotation sensor include a high optical dynamic range, real-time image processing, and a wide range of detectable angular velocity. The proposed rotation sensor is appropriate for applications like the real-time and remote detection of the rotation of automobile engines and wheels, motors, microscopic rotating images, etc.

An experimental chip was designed and fabricated by a 0.6-μm single-poly-triple-metal CMOS process. The total chip area was $1812 \times 1825 \, \mu\text{m}^2$. The area of a single pixel was $91 \times 84 \, \mu\text{m}^2$ with a fill factor of 20%. The dc power consumption was 10 mW at 5 V in the dark. The experimental

The authors are with the Department of Electronics Engineering, National Chiao Tung University, Hsinchu, 300 Taiwan, R.O.C. (e-mail: khhuang@faraday-tech.com.tw; m8711575@alab.ee.nctu.edu.tw; cywu@alab.ee.nctu.edu.tw).
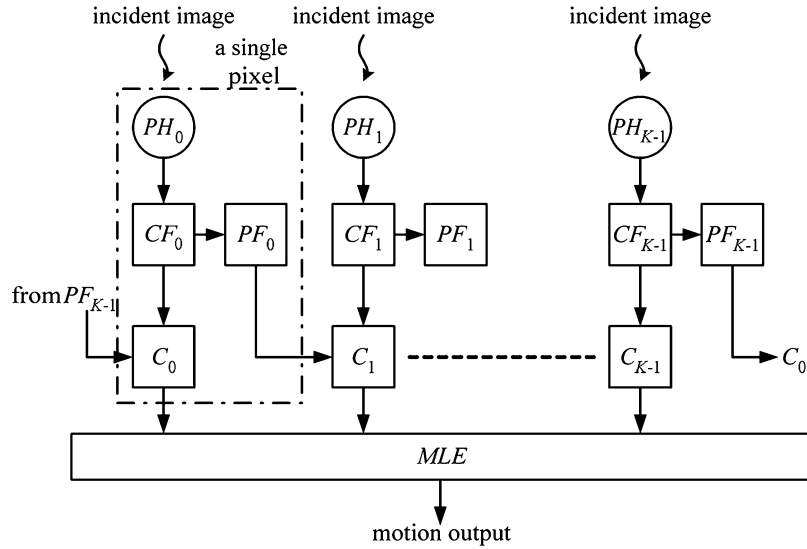
Fig. 1.   Conceptual structure of the adopted correlation-based algorithm for rotation detection. Each pixel is comprised of a retinal processing circuit PH, registers CF and PF, and correlator C. MLE aggregates the output of all correlators in a single circle to determine the global rotation.

results of the fabricated chip confirmed that both the clockwise and counterclockwise directions can be accurately detected. The angular velocity selectivity was also verified at angular velocities from $2.5 \times 10^{-3} \ \pi/\mathrm{s}$ to $40 \ \pi/\mathrm{s}$. By sweeping the clock rate, the proposed rotation sensor can be used to detect a range of angular velocities from $2 \times 10^{-2} \ \pi/\mathrm{s}$ to $206 \ \pi/\mathrm{s}$. The optical dynamic range at a contrast of 80% was 52 dB, from 0.91 to 366 lux.

Section II analyzes the method of detecting rotation. Section III shows the architecture of the proposed rotation sensor. Section IV presents the experimental results and, finally, the Conclusion is presented.

II. ROTATION DETECTION METHOD

In most correlation-based motion sensors, the pixels are regularly distributed in a rectangular pattern and each pixel is correlated with the delayed photo inputs of the adjacent pixels to determine the local motion vectors. However, if the incident image is rotated, the tangential velocity is proportional to the radius. For the motion sensors with regularly and rectangularly distributed pixels, the delay time, which determines the local velocity to be detected, must be adjusted according to the radius in order to detect the tangential velocity. A motion sensor cannot easily adjust all the local delay times of each pixel to detect rotation. Moreover, even if all the local delay times could be generated, mapping must be performed from Cartesian coordinates to polar coordinates to detect angular velocities and directions. The pixels in the proposed rotation sensor are arranged in a polar structure to detect the rotation, and, thus, resolve these problems. Instead of generating the desired delay times for each pixel, the pixels are placed on a circle, with an equal angular spacing, so that the distance between two adjacent pixels is proportional to the radius of rotation, and the delay time is thus the same for all pixels.

The conceptual structure of the adopted correlation-based algorithm for detecting rotation is shown in Fig. 1, where there are K pixels in a circle. A single pixel consists of both photo sensing

and signal processing units, to form a focal-plane motion sensor. The retinal processing circuit PH includes the retinal smoothing network [8], [10], [11], a photoreceptor, a current-input Schmitt trigger [12], and an inverter. The retinal smoothing network is used to extract the local spatial and temporal averages of the input images. The photoreceptor senses the input images. The output currents of the retinal smoothing network and the photoreceptor are sent to the current-input Schmitt trigger, which amplifies the difference between the two input currents with hysteresis. The output of the current-input Schmitt trigger is a voltage signal and is further amplified to VDD and VSS by the inverter. The output image of PH is a black-and-white image. In the black region, the output voltage of the retinal processing circuit will be VSS, which is logic zero, whereas in the white region, the output voltage will be VDD, which is logic one. The output voltage of PH is sampled at the rising edge of the clock signal and is stored in the register CF. The data in CF is shifted to the register PF after a clock period. The two registers CF and PF are used to store current and previous image frames. The output of PF is then sent to the correlator C of the pixel in the preferred direction. The delay time is determined by the period of the clock signal, which can be precisely adjusted to detect wide range of angular velocities, independent of the process variation [8]. If the clock period equals the time for which the incident image moves from one pixel to the next pixel, then the two inputs of the correlator will be the same and the output of the correlator will be at logic one. The appearance of logic one indicates that a selected local motion vector is detected. MLE is used to aggregate the outputs of all correlators in a single circle, to determine the velocity and direction of the global rotation. MLE is implemented using a NAND gate, so the output of MLE is logical zero if the outputs of all correlators are at logic one.

A. Analysis of Angular Velocity Selectivity for a Single-Edged Image

The angular velocity selectivity of a single-edged image is initially analyzed and generalized to the image with more than
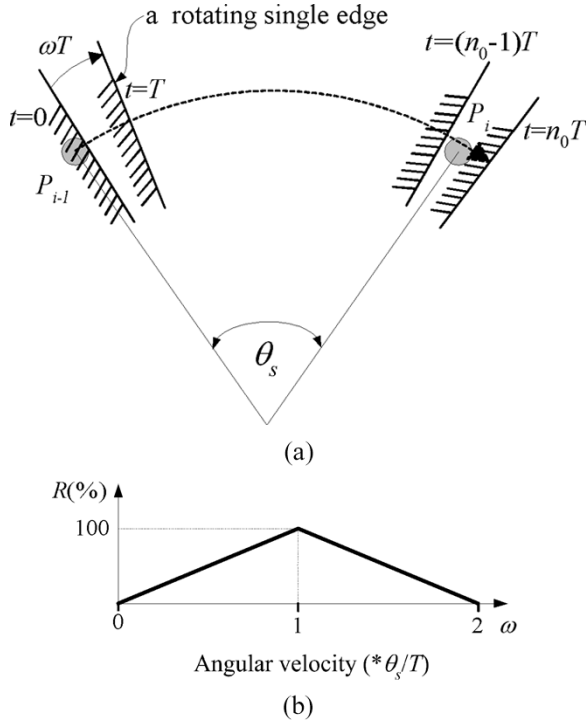
Fig. 2. (a) An edge, rotating from the $(i-1)$th pixel P_{i-1} to the ith P_i pixels within n_0 clock cycles. θ_s is the angle between two correlated pixels. ω is the angular velocity and T is the clock period. (b) The relationship between R and ω, where R is defined as the ratio of the number of times when the output of MLE is at logic 0 in N clock cycles, to N.

one edge. A single edge is rotated clockwise from the $(i-1)$th pixel P_{i-1} to the ith pixel P_i within n_0 clock cycles, as shown in Fig. 2(a), where P_{i-1} and P_i are the two adjacent and correlated pixels in the same circle and θ_s is the angle between the two correlated pixels. The region behind the edge is black as shown in Fig. 2(a). In Fig. 2(a), the edge is rotated clockwise by an angle of ωT in a clock cycle, where ω is the angular velocity and T is the clock period. In computing the output of MLE at any clock cycle, only the two correlated pixels that are next to the edge, i.e. P_{i-1} and P_i in Fig. 2(a), are significant in determining the output of MLE during any clock cycle because the pixels that are not next to the edge are either in the black or the white region, so the data stored in CF and PF of these pixels are the same, and the correlation results for these pixels are always at logic one. Thus, the correlation results for these pixels do not influence the output of MLE.

If ωT does not exceed θ_s, this edge is approaching to P_i by an angle of ωT in a clock cycle. During these clock cycles, the output of the correlator of P_{i-1} is maintained at logic one while the output of the correlator of P_i is at logic zero. The output of the correlator of P_i becomes logic one at $t = n_0 T$ when the edge moves over P_i. The output of MLE becomes logic zero at $t = n_0 T$. Since the angle between P_{i-1} and P_i is θ_s and the edge approaches P_i by an angle ωT in a clock cycle, the period for which the MLE outputs logic zero is $n_0 = \theta_s/\omega T$ clock cycles. For example, if the edge moves from P_{i-1} with an angular velocity of $\theta_s/5T$, the outputs of the correlators of P_{i-1} and P_i in five successive clock clocks are $\{1,1,1,1,1\}$ and $\{0,0,0,0,1\}$. The output of MLE is $\{1,1,1,1,0\}$ and the period n_0 is five.

If the angular velocity of the rotating image exceeds θ_s/T, the edge will move over P_i in every clock cycle. However, this edge approaches P_{i+1} by an angle of $\omega T - \theta_s$ in every clock cycle. Once this edge reaches P_{i+1}, a correlation result of logic zero is generated at P_{i+1} and the output of MLE is at logic one. The period during which the MLE outputs logic one is $n_1 = \theta_s/(\omega T - \theta_s)$ clock cycles. For example, if ωT is $6\theta_s/5$, then the correlation outputs of P_{i-1}, P_i, and P_{i+1} in five successive clock cycles are $\{1,1,1,1,1\}$, $\{1,1,1,1,1\}$ and $\{1,1,1,1,0\}$, respectively. The output of MLE is $\{0,0,0,0,1\}$ so n_1 is five.

The ratio R is defined as the ratio of the number of times for which the output of MLE is at logic zero during N clock cycles to N. If ωT does not exceed θ_s, since the period for which the MLE outputs logic zero is $n_0 = \theta_s/\omega T$ clock cycles, q_0 MLE outputs of logic zero occur within N clock cycles, where q_0 is the quotient N/n_0. If r_0 is the remainder of N/n_0, $N = q_0 n_0 + r_0$. According to the definition of R, R can be expressed by

$$R(\%) \equiv \frac{100 q_0}{N} = \frac{100(N - r_0)}{n_0 N}$$
$$= 100\left(\frac{1}{n_0} - \frac{r_0}{n_0 N}\right) \quad 0 \le \omega \le \frac{\theta_s}{T}. \qquad (1)$$

If N is large, the ratio R can be approximated as

$$R(\%) \cong \frac{100}{n_0} = \frac{100 \omega T}{\theta_s} \quad 0 \le \omega \le \frac{\theta_s}{T}. \qquad (2)$$

If ωT is greater than θ_s, then the period for which the MLE output is logic one is $n_1 = \theta_s/(\omega T - \theta_s)$ clock cycles. Thus, q_1 MLE outputs of logic one occur within N clock cycles, where q_1 is the quotient of N/n_1. If r_1 is the remainder of N/n_1, $N = q_1 n_1 + r_1$. According to the definition, R can be expressed by

$$R(\%) \equiv 100 \frac{N - q_1}{N} = 100\left(1 - \frac{N - r_1}{n_1 N}\right)$$
$$= 100\left(1 - \frac{1}{n_1} + \frac{r_1}{n_1 N}\right) \quad \frac{\theta_s}{T} \le \omega \le \frac{2\theta_s}{T}. \qquad (3)$$

If N is large, the ratio R can be approximated as

$$R(\%) \cong 100\left(1 - \frac{1}{n_1}\right)$$
$$= 100\left(1 - \frac{\omega T - \theta_s}{\theta_s}\right) \quad \frac{\theta_s}{T} \le \omega \le \frac{2\theta_s}{T}. \qquad (4)$$

Fig. 2(b) plots the relationship between R and angular velocity. R is maximum at θ_s/T, which can be controlled by the period T of the clock signal. Notably, R is also maximum at $\omega = \theta_s/T + b(2\pi/T)$, where b is a arbitrary integer, due to the aliasing effect.

B. Analysis of Angular Velocity Selectivity for Multiple-Edged Image

The above analysis concerns a single edge. In practice, the incident image always has more than one edge. Angular velocity selectivity is influenced by the number and positions of the edges. The following analysis is based on the assumption
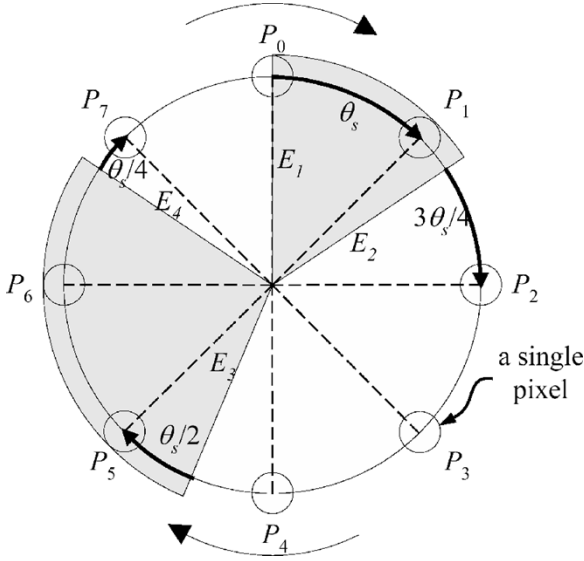
Fig. 3. Example of an image with four edges located in various positions, rotating clockwise. There are eight pixels, P_0 to P_7. The image has four edges E_1, E_2, E_3, and E_4 and the initial angles between these edges and their own front pixels are θ_s, $3\theta_s/4$, $\theta_s/2$, and $\theta_s/4$, respectively.

that there is no more than one edge existing between two adjacent pixels. If the image has several edges, every edge has to move across the pixel that lies in front of the edge, for example P_i in Fig. 2(a), in a single clock cycle to yield a logic zero at the MLE output. If the angular velocity is θ_s/T, then R equals 100%. However, if the edges are not exactly rotated by θ_s in a clock cycle, the time taken by an edge to move across its own front pixel is different for different edge since the initial positions of the edges are different.

Fig. 3 illustrates how the initial positions of the edges affect the time taken by an edge to move across its own front pixel. There are eight pixels, P_0 to P_7, in a circle. The image has four edges E_1, E_2, E_3, and E_4 and the initial angles θ_{ep} between these edges and their own front pixels are θ_s, $3\theta_s/4$, $\theta_s/2$, and $\theta_s/4$, respectively. If the angular velocity is $3\theta_s/4T$, the front pixel of E_1 is P_1, P_1, P_2, and P_3 for the first, second, third, and fourth clock cycles, respectively. Thus, the pattern of correlation outputs at the front pixels of E_1 in the first four clock cycles is $\{0,1,1,1\}$. For E_2, E_3, and E_4, the patterns of correlation outputs at their front pixels during the first four clock cycles are $\{1,0,1,1\}$, $\{1,1,0,1\}$, and $\{1,1,1,0\}$, respectively. Each set of correlation output patterns periodically repeats. This example indicates that the different values of θ_{ep} result in a time difference between the occurrences of logic zero in the correlation output patterns of the front pixels. The resultant MLE outputs during the first four clock cycles are $\{1,1,1,1\}$ and R is zero. If θ_{ep} is the same for every edge, then the time taken by every edge to move across its own front pixel is the same, so it is similar with the single-edged case. Thus, the correlation output patterns are the same for every edge and are one of $\{0,1,1,1\}$, $\{1,0,1,1\}$, $\{1,1,0,1\}$, and $\{1,1,1,0\}$. The output of MLE is $\{1,0,0,0\}$, $\{0,1,0,0\}$, $\{0,0,1,0\}$, or $\{0,0,0,1\}$ and R is 75%, which is the value derived from (2) with $\omega = 3\theta_s/4T$.

If we consider a single edge, the number of times for which correlation output is at logic one during N clock cycles is the

same as that for which the MLE output is at logic zero during N clock cycles, which can be calculated from (2) as $N\omega T/\theta_s$, if ω is less than θ_s/T. In the multiple-edged case, every edge generates $N\omega T/\theta_s$ times of logic one at the correlation output of its front pixels within N clock cycles. For example, if $N = 4$, E_1 generates logic one at the output of correlator $4(3\theta_s/4T)T/\theta_s = 3$ times. The same number can be also calculated from the correlation output pattern of E_1 $\{0,1,1,1\}$ as three. Thus, for each edge, there are $N - N\omega T/\theta_s$ times of logic zero at the correlation output of its front pixels during N clock cycles. The above example of Fig. 3 shows that the different values of θ_{ep} cause the logic zero of correlation output of the front pixels to occur at different time. If the image has L edges and the values θ_{ep} for all of the edges are equally distributed within θ_s, as in the above example of Fig. 3, logic zero appears at the correlation outputs of the front pixel for L edges in turn. The output of MLE is logic one if one of the outputs of the correlators is at logic zero. Thus, the number of times for which the output of MLE is logic one during N clock cycles is $L(N - N\omega T/\theta_s)$. According to the definition of R, R is given by

$$R(\%) = 100 \frac{\left[N - L\left(N - \frac{N\omega T}{\theta_s} \right) \right]}{N}$$
$$= \frac{100L\left(\omega T - \frac{L-1}{L}\theta_s \right)}{\theta_s} \quad \frac{(L-1)\theta_s}{LT} \le \omega \le \frac{\theta_s}{T}. \quad (5)$$

According to (5), R is decreased to zero at $\omega = \theta_s(L-1)/LT$ and increased to 100% at $\omega = \theta_s/T$. If ω exceeds θ_s/T, a similar analysis can be performed to obtain the relationship between R and ω as

$$R(\%) = 100 \left[1 - \frac{L(\omega T - \theta_s)}{\theta_s} \right] \quad \frac{\theta_s}{T} \le \omega \le \frac{(L+1)\theta_s}{LT}. \quad (6)$$

R falls to zero at $\omega = \theta_s(L+1)/LT$ and increases to 100% at $\omega = \theta_s/T$.

If θ_{ep} is the same for every edge, the time when every edge moves across its own front pixel is the same, so the relationship between R and ω is the same as in the single-edged case. The relationship between R and ω is given by (2) and (4).

The above two extreme cases of θ_{ep} set the maximum and minimum values of R at every ω. Fig. 4(a) presents the relationship between R and ω for arbitrary position of the edges. R is confined to the shaded region, defined by (2), (4), (5), and (6).

MATLAB simulations were performed by rotating the image clockwise, and the outputs of MLE were recorded over 100 successive clock cycles, such that $N = 100$, to compute R. ω was swept from 0 to $2\theta_s/T$ to obtain the curve of R versus ω. Simulations were performed with various numbers of edges in various positions. Fig. 4(b) and (c) shows the simulation results for $L = 2$ and $L = 4$, respectively, where L is the number of edges. The angles θ_{ep} for every edge are the same for curve 1 in Fig. 4(b) and (c). As can be seen from Fig. 4(b) and (c), the relationship between R and ω depicted by curve 1 is consistent with (2) and (4). For curve 2 in Fig. 4(b), θ_{ep} is set to θ_s and $\theta_s/2$ and for curve 2 in Fig. 4(c), it is set to θ_s, $3\theta_s/4$, $\theta_s/2$ and $\theta_s/4$. The relationship between R and ω represented by curves 2 in
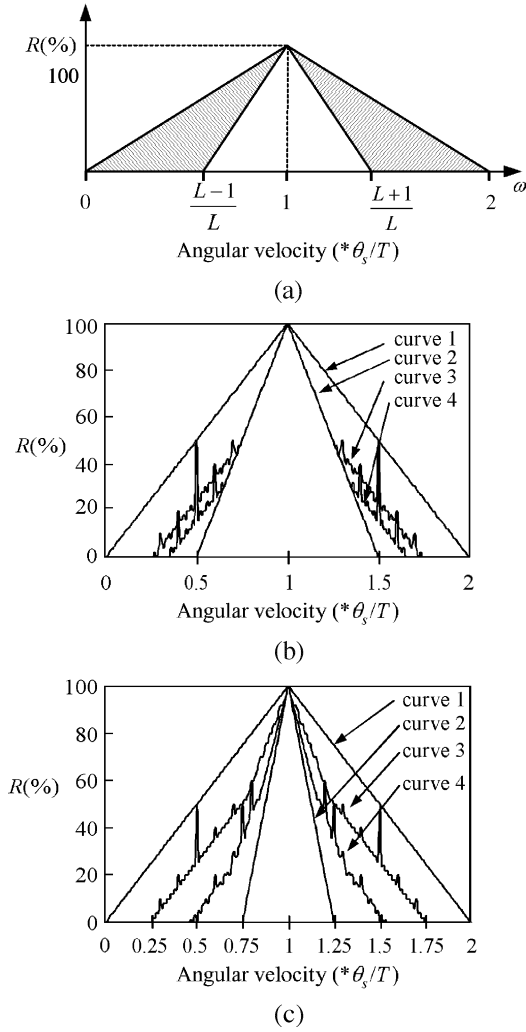
Fig. 4. (a) Relationship between R and ω for an image with L edges located at various positions. (b) MATLAB simulation results with $L = 2$. (c) MATLAB simulation results with $L = 4$. Curves 1 and 2 refer to the extreme cases in which R is maximum and minimum at every ω, respectively. Curves 3 and 4 refer to the simulation results with random $\theta_{\rm ep}$ for every edge.

Fig. 5. (a) Structure modified to enhance the angular velocity selectivity. A total of a pixels are placed within θ_s while the two pixels separated by θ_s are correlated. (b) Example of an edge's approaching the ath pixel P_a. The edge crosses P_a at the n_0th clock cycle. (c) Relationship between ω and R for the modified structure.

Fig. 4(b) and (c) are consistent with (5) and (6) with $L = 2$ and $L = 4$, respectively. Curves 3 and 4 in Fig. 4(b) and (c) plot the simulation results with random $\theta_{\rm ep}$ for every edge. These figures show that curves 3 and 4 are confined by curves 1 and 2, while there are some peaks in curves 3 and 4, because R is not linearly proportional to ω for certain $\theta_{\rm ep}$ values. The nonlinearity arises because the operation of MLE, which is the logical operation of NAND, is not linear. However, in the above two extreme cases, the corresponding $\theta_{\rm ep}$ does not cause peaks. The simulation was performed $160\,000$ kinds of $\theta_{\rm ep}$ values and all $160\,000$ curves were verified to be confined within curves 1 and 2.

C. Analysis of Angular Velocity Selectivity With a Modified Structure

Equations (2) and (4) imply that MLE output of logic zero is generated only if the images are rotated with the angular velocities ranging between 0 and $2\theta_s/T$. To further enhance the angular velocity selectivity, the range of angular velocities that generate the logic zero at MLE outputs should be confined to be narrower than $2\theta_s/T$. Fig. 5(a) shows a modified structure
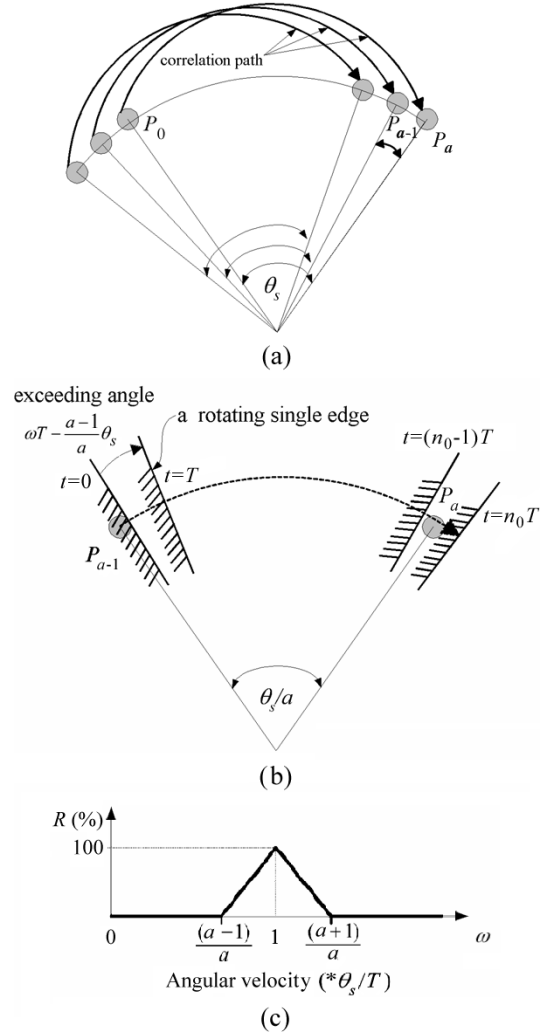
intended to enhance the angular velocity selectivity. The modified structure includes a pixels rather than one pixel within θ_s while the correlation is still performed on the two pixels that are θ_s apart. The number of pixels in a circle is thus increased by a factor of a. In the original structure in Fig. 2(a), the correlation result of P_i has to be at logic one in order to obtain an MLE output of logic zero. In the modified structure, the correlation results of all the a pixels from P_1 to P_a within θ_s must be at logic one to yield an MLE output of logic zero, where P_0 is defined as the pixel that is just behind the edge at the beginning of every clock cycle. Consequently, the edge has to move across a pixels from P_1 to P_a in a clock cycle to ensure all a pixels have a correlation result of logic zero. If ωT is less than $(a-1)\theta_s/a$, then the number of pixels crossed by the edge during a clock cycle is always less than a, so the output of MLE is always logic one. If ωT is greater than $(a-1)\theta_s/a$, then MLE begins to output logic zero.

Fig. 5(b) presents an example in which the angular velocity selectivity is analyzed. Since ωT is greater than $(a-1)\theta_s/a$, then the edge can cross $a-1$ pixels from P_1 to P_{a-1} in each

clock cycle and exceed P_{a-1} by an angle of $\omega T - (a-1)\theta_s/a$ in every clock cycle. The exceeding angle is accumulated during successive clock cycles until the edge crosses P_a. An MLE output of logic zero is generated whenever the edge crosses a pixels from P_1 to P_a in a clock cycle. Since the angle between P_{a-1} and P_a is θ_s/a, the period for which an MLE output of logic zero appears is $n_0 = (\theta_s/a)/(\omega T - (a-1)\theta_s/a)$ clock cycles. As in the derivations of (1) and (2), R can be approximated by $100/n_0 = 100(\omega T - (a-1)\theta_s/a)/(\theta_s/a)$ if N is large. A similar analysis can be also performed for the case in which ωT is greater than θ_s and less than $(a+1)\theta_s/a$. In such a case, R can be derived as $100(1 - a(\omega T - \theta_s)/\theta_s)$ if N is large. The relationship between R and angular velocity for the modified structure can be summarized as

$$R(\%) = \begin{cases} \frac{100a\left(\omega T - \frac{a-1}{a}\theta_s\right)}{\theta_s}, & \frac{(a-1)\theta_s}{aT} \leq \omega \leq \frac{\theta_s}{T} \\ 100\left[1 - \frac{a(\omega T - \theta_s)}{\theta_s}\right], & \frac{\theta_s}{T} \leq \omega \leq \frac{(a+1)\theta_s}{aT} \end{cases}. \quad (7)$$

Fig. 5(c) plots R versus ω from (7). Fig. 5(c) indicates that the range of the angular velocities that generate logic zero at MLE output is confined to only $2\theta_s/aT$ so the angular velocity selectivity is enhanced.

If the images have more than one edge, an analysis similar to that in Section II-B can be performed. The relationship between R and ω is given by

$$0 \leq R(\%) \leq \frac{100a\left(\omega T - \frac{a-1}{a}\theta_s\right)}{\theta_s}$$
$$\frac{(a-1)\theta_s}{aT} \leq \omega \leq \frac{(aL-1)\theta_s}{aLT}$$
$$\frac{100aL\left(\omega T - \frac{aL-1}{aL}\theta_s\right)}{\theta_s} \leq R(\%) \leq \frac{100a\left(\omega T - \frac{a-1}{a}\theta_s\right)}{\theta_s}$$
$$\frac{(aL-1)\theta_s}{aLT} \leq \omega \leq \frac{\theta_s}{T}$$
$$100\left[1 - \frac{aL(\omega T - \theta_s)}{\theta_s}\right] \leq R(\%) \leq 100\left(1 - \frac{a(\omega T - \theta_s)}{\theta_s}\right)$$
$$\frac{\theta_s}{T} \leq \omega \leq \frac{(aL+1)\theta_s}{aLT}$$
$$0 \leq R(\%) \leq 100\left(1 - \frac{a(\omega T - \theta_s)}{\theta_s}\right)$$
$$\frac{(aL+1)\theta_s}{aLT} \leq \omega \leq \frac{(a+1)\theta_s}{aT}. \quad (8)$$

Fig. 6(a) plots R against ω, according to (8). R is confined to the shaded region. Equation (8) implies that a alone determines the maximum value of R at every ω whereas both a and L determine the minimum value of R at every ω. Fig. 6(b) shows the MATLAB simulation results with $a = 2$ and $L = 16$. The angles θ_{ep} for every edge are the same for curve 1 in Fig. 6(b). As can be seen from Fig. 6(b), the relationship between R and ω depicted by curve 1 is given by (2) and (4). The θ_{ep} values are $m\theta_s/32T$, $m = 1, 2, \ldots, 16$, for curve 2, which describes the extreme case in which R is set to a minimum value at every ω. Curves 3 and 4 plot the simulation results with random θ_{ep} values for every edge. Fig. 6(b) indicates that curves 3 and 4 are confined within curves 1 and 2.
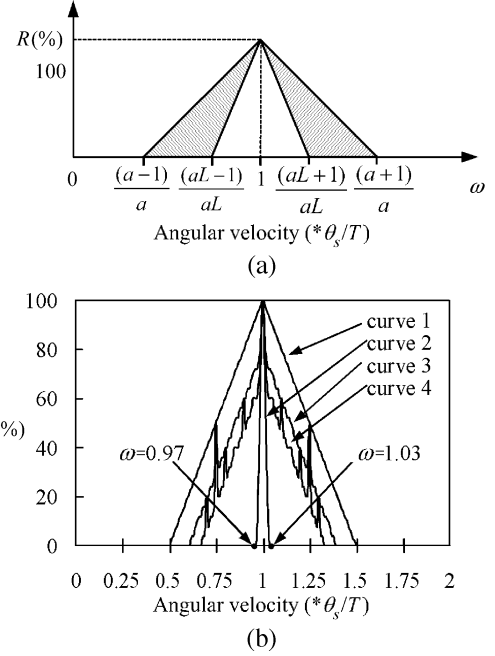

Fig. 6. (a) Relationship between R and ω for the modified structure when the image has L edges at arbitrary positions. (b) MATLAB simulation results with $a = 2$ and $L = 16$. Curves 1 and 2 are the extreme cases in which R is maximum and minimum at every ω, respectively. Curves 3 and 4 are the simulation results with random θ_{ep} for every edge.
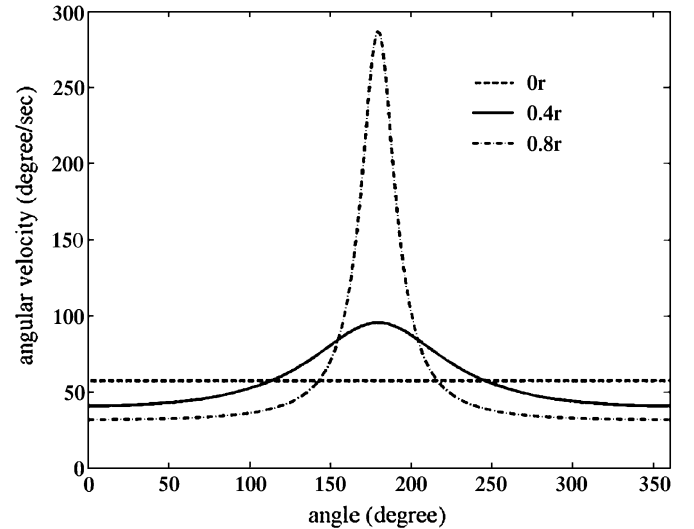

Fig. 7. Angular velocity versus angle with the center of rotation shifted in the $0°$ direction by 0, $0.4r$, and $0.8r$, where r is the radius of the circle of pixels.

D. Analysis of Misalignment Effect

The angular velocity selectivity is degraded if the center of the rotating image is not precisely aligned to the center of the circle of the pixels. Fig. 7 shows the angular velocity under the condition that the center of rotation is shifted in the $0°$ direction with r_n values of 0, 0.4, and 0.8, where r_n is the ratio of the shifted distance r_s to the radius of the circle of the pixels, r. The angular velocity of rotation is fixed at $62.8°/s$. As can be seen in Fig. 7, the deviation in angular velocity from $62.8°/s$ increases with r_n. This misalignment degrades the angular velocity selectivity. When the image is rotated with an angular velocity of
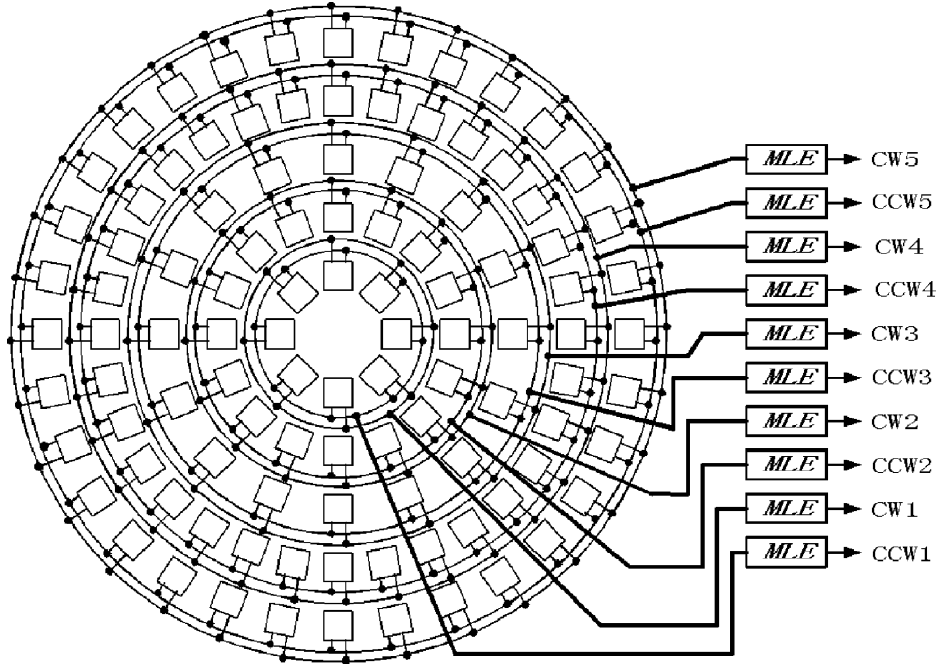
Fig. 8. Architecture of the proposed rotation sensor, which includes104 pixels in five concentric circles. The clockwise and the counterclockwise correlation results of all the pixels in a single circle are sent to MLE.
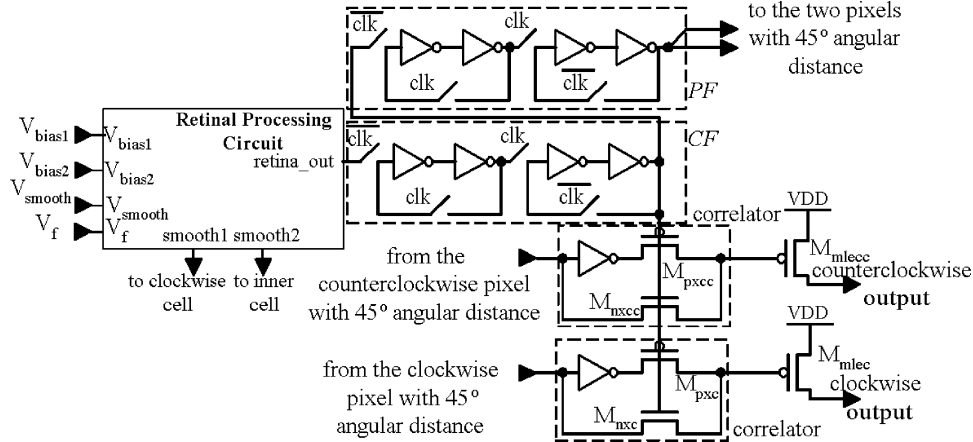

Fig. 9. Pixel structure of the rotation sensor. Each pixel consists of a retinal processing circuit, two registers CF and PF, two correlators, and two P-channel MOSFETs M_{mlecc} and M_{mlec}, which are parts of MLE, implemented by NAND gates.

θ_s/T, the theoretical maximum R is 100%. However, due to the misalignment effect, the angular velocity deviates from θ_s/T so that the maximum R falls as r_n increases. On the other hand, if the angular velocity is greater than $(a + 1)\theta_s/(aT)$, then the theoretical value of R should be zero, as shown in Fig. 6(a). However, since the angular velocity is decreased at part of the circle of the pixels, the MLE output may be logic zero when the edges move across this part. The angular velocity selectivity is thus degraded. If r_s is fixed, then the misalignment effect can be reduced by increasing r.

III. ARCHITECTURE AND CIRCUIT

The pixels are placed in a circular arrangement to detect rotation. Fig. 8 presents the architecture of the proposed rotation sensor, which is comprised of 104 pixels, which form five concentric circles. The radii of the circles are 127.4, 254.55, 387.55, 523.5, and 671.9 μm in order from the center. The numbers of

pixels in the five circles are 8, 16, 16, 32, and 32, and the angles between the adjacent pixels are fixed at 45°, 22.5°, 22.5°, 11.25°, and 11.25°, respectively. Every pixel is correlated with the clockwise and counterclockwise pixels that are 45° apart; that is, $\theta_s = 45°$. The clockwise or the counterclockwise correlation results of all the pixels in the same circle are sent to MLE. MLE is implemented using a NAND gate. Two sets of MLEs are involved, corresponding to clockwise and counterclockwise rotation, for a single circle. CW1, CW2, CW3, CW4, and CW5 in Fig. 8 are the clockwise outputs of the MLEs of the first, second, third, fourth, and fifth circles, while CCW1, CCW2, CCW3, CCW4, and CCW5 are the counterclockwise outputs of the MLEs of the first, second, third, fourth, and fifth circles, respectively. The proposed rotation sensor includes a total of ten sets of MLEs.

Fig. 9 shows the structure of a single pixel. Each pixel consists of a retinal processing circuit, two registers, two correlators and two P-channel MOSFETs, which are parts
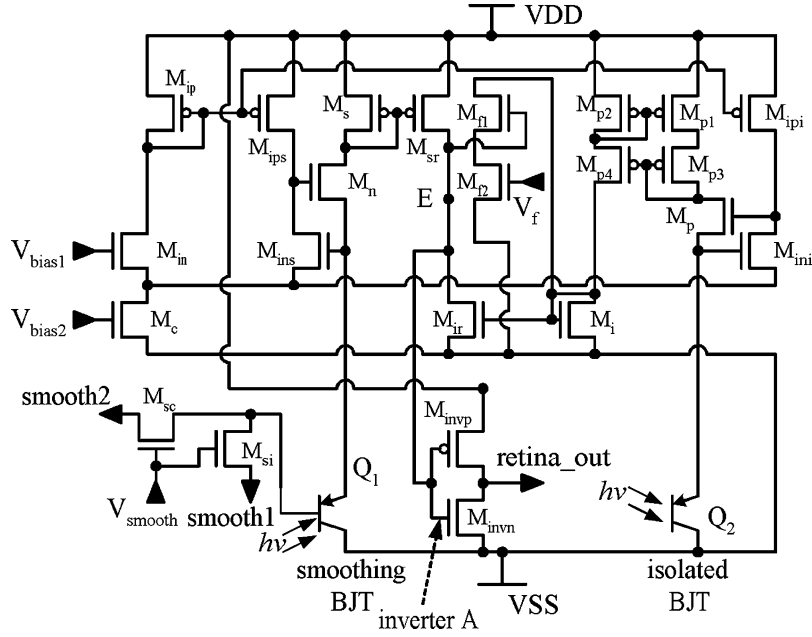
Fig. 10.   Structure of the retinal processing circuit. The retinal processing circuit includes an isolated photo-BJT Q_2, a smoothing photo-BJT Q_1, a current-input CMOS Schmitt trigger, and an inverter.

TABLE I
SIZE OF THE TRANSISTORS OF THE RETINAL PROCESSING CIRCUITS

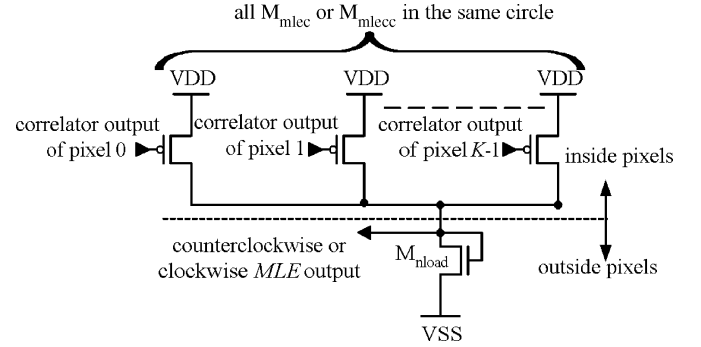|	W (μm)	L (μm)
M_c	1.5	1.2
$M_{ip}=M_{ips}=M_{ipi}$	1.5	1.2
$M_{in}=M_{ins}=M_{ini}$	3	1.2
$M_p=M_n$	1.5	0.6
$M_s=M_{sr}=M_i=M_{ir}$	4.5	2.4
$M_{f1}=M_{f2}$	1.5	0.6
$M_{p1}=M_{p2}=M_{p3}=M_{p4}$	9	3
$M_{sc}=M_{si}$	1.5	0.6
M_{invp}	1.5	0.6
M_{invn}	1.5	0.6

Fig. 11.   Structure of MLE, which is implemented by a NAND gate with a fan-in number equal to the number of pixels in a circle.

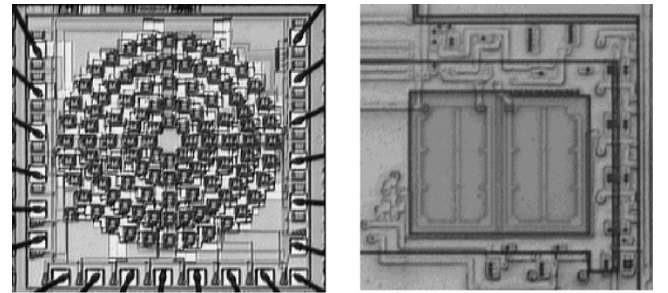Fig. 12.   Photograph of (a) the whole chip and (b) a single pixel, of the rotation sensor.

of the NAND gates that form MLE. The dimensions of the transistor M_{nxcc}, M_{nxc}, M_{pxcc}, M_{pxc}, M_{mlecc}, and M_{mlec} are $W/L = 1.5/0.6$ (μm). Fig. 10 depicts the retinal processing circuit, which includes an isolated photo-BJT Q_2 used as a photoreceptor, a smoothing photo-BJT Q_1 with adjustable N-channel MOSFET resistors used as the retinal smoothing network, a current-input CMOS Schmitt trigger, and an inverter. The base of the smoothing photo-BJT Q_1 is connected to the bases of the smoothing photo-BJT in the four nearest neighbors, in both θ and r directions, via the N-channel MOSFET resistors M_{sc} and M_{si}, whose resistance is controlled by the gate voltage V_{smooth}. The transistors M_{ins}, M_{ips}, M_{ini}, M_{ipi}, M_n, M_p, M_{ip}, M_{in}, and M_c are used to virtually bias the emitters of Q_1 and Q_2 at V_{bias1}. The current-input CMOS Schmitt trigger comprises of M_s, M_{sr}, M_i, M_{ir}, M_{f1}, and M_{f2} transistors. The voltage V_f is used to adjust the threshold level of the current-input CMOS Schmitt trigger. The transistors M_{p1}, M_{p2}, M_{p3}, and M_{p4} are used to mirror the emitter current

of Q_2 to the current-input CMOS Schmitt trigger. The inverter A amplifies the output of the current-input CMOS Schmitt trigger to VDD or VSS. The size of the transistors of the retinal processing circuit is summarized in Table I.

As shown in Fig. 9, two registers are used to store the output of the retinal processing circuit at the current and the previous clock cycles. The register CF samples and stores the output of
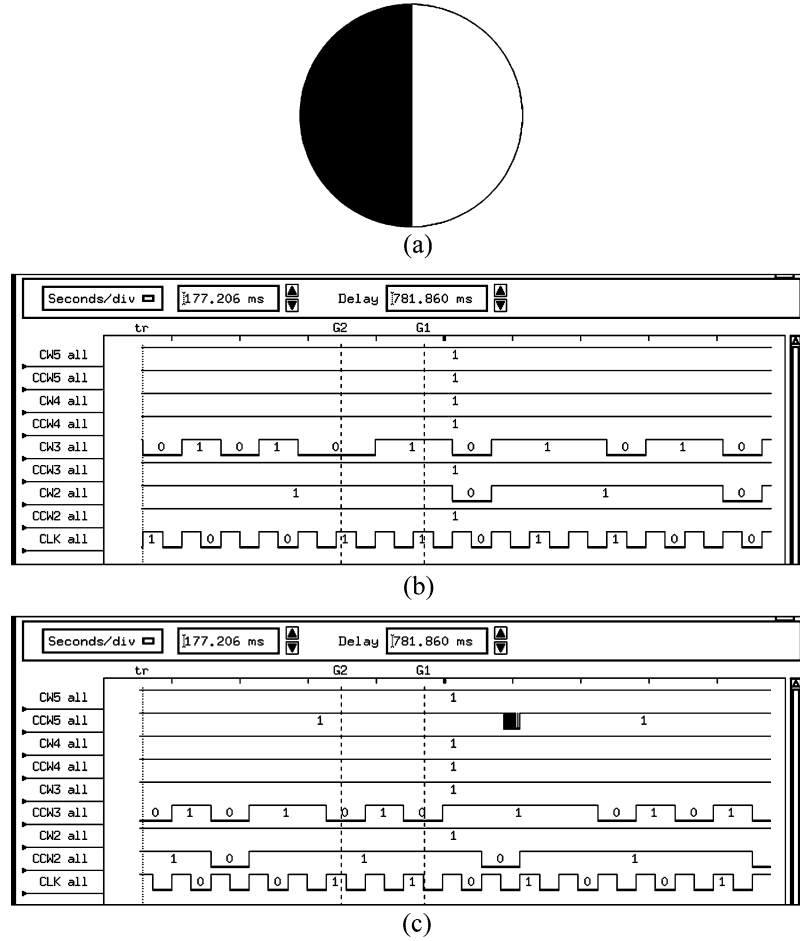
Fig. 13. (a) Pattern used to test rotation direction selectivity. (b) Waveforms measured by the logic analyzer with the image rotated clockwise. (c) Waveforms measured by the logic analyzer with the image rotated counterclockwise. The waveforms, CW2 (CCW2), CW3 (CCW3), CW4 (CCW4), and CW5 (CCW5) are the clockwise (counterclockwise) outputs of MLE of second, third, fourth, and fifth circles. The contrast of the pattern is 99% and the light source is a 5-mW LASER. The clock rate is 10 Hz and the angular velocity is 2.5 $\pi/$s.

the retinal processing circuit at the rising edge of every clock cycle. The data stored in the register CF is shifted to the register PF after a clock cycle. The output of register CF is sent to the correlators of the pixel itself, whereas the output of register PF is sent to the correlators of the two correlated pixels, which are $45°$ apart in clockwise and the counterclockwise directions. The output of register CF is correlated with the outputs of register PF of the two pixels, which are $45°$ apart in the clockwise and counterclockwise directions. The two correlators correspond to detect clockwise and counterclockwise rotations, respectively. The correlators are implemented using XNOR gates. If the two inputs of the correlators are the same, then the correlation output is at logic one.

Fig. 11 shows the structure of MLE, which is implemented by a NAND gate with a fan-in number equal to the number of pixels in a circle. The P-channel MOSFETs of the NAND gate are located inside each pixel, which are the MOSFETs $\mathrm{M_{mlecc}}$ and $\mathrm{M_{mlec}}$ in Fig. 9. The outputs of the correlators in each pixel are sent to the gates of $\mathrm{M_{mlecc}}$ and $\mathrm{M_{mlec}}$, as shown in Fig. 9. The drains of $\mathrm{M_{mlecc}}$ ($\mathrm{M_{mlec}}$) of every pixel in a single circle are connected together to the diode-connected N-channel MOSFET $\mathrm{M_{nload}}$, which acts as the load to generate the counterclockwise (clockwise) MLE output. The dimension of the

transistor $\mathrm{M_{nload}}$ is $\mathrm{W/L} = 1/15$ $(\mu\mathrm{m})$. If one of the outputs of the correlators is at logic zero, then the output of MLE is at logic one. If the outputs of the correlators of every pixel in a single circle are at logic one, the output of MLE is at logic zero.

IV. EXPERIMENTAL RESULTS

An experimental focal-plane rotation sensor chip was fabricated in a 0.6 μm single-ploy-triple-metal CMOS process. The resultant chip area was 1812×1825 $\mu\mathrm{m}^2$ and the area of a single pixel was 91×84 $\mu\mathrm{m}^2$, with a fill factor of 20%. The dc power consumption was 10 mW at 5 V in the dark. Fig. 12 shows photographs of the whole chip and a single pixel.

A pattern shown in Fig. 13(a) was used to verify the direction selectivity. The contrast of the pattern was 99% and the light source was a 5-mW LASER, which was used in all of the following experiments, except where specified. The contrast is computed as $(\mathrm{I_{white}} - \mathrm{I_{black}})/(\mathrm{I_{white}} + \mathrm{I_{black}})$, where $\mathrm{I_{black}}$ and $\mathrm{I_{white}}$ are the induced photocurrents at the black and white regions, respectively. A lens was used to focus the image on the area that covers the three inner circles for good alignment. The clock frequency was 10 Hz and the angular velocity was 2.5 $\pi/$s. Fig. 13(b) and (c) show the output waveforms, measured by a
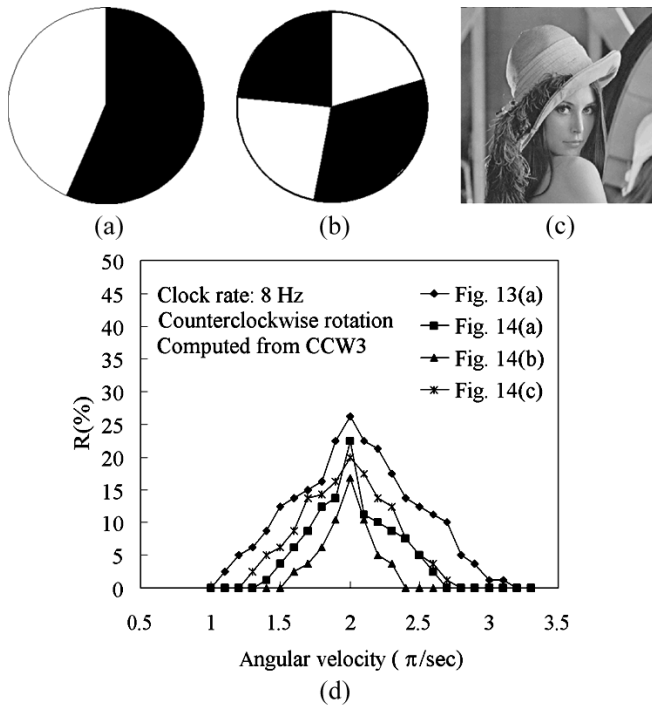
Fig. 14. (a) Test pattern with θ_{ep} of 11.25° and 22.5°. (b) Test pattern with θ_{ep} of 0°, 5.125°, 11.25°, and 16.375°. (c) Test pattern, Lena. (d) Angular velocity selectivity with the four patterns in Figs. 13(a) and 14(a)–(c).
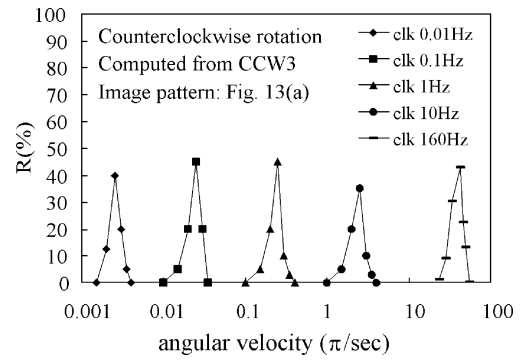

Fig. 15. Relationship between R and ω at clock rates of 0.01, 0.1, 1, 10, and 160 Hz. Angular velocities when R is maximum are at 0.0025, 0.025, 0.25, 2.5, and 40 π/s.

logic analyzer. The image was rotated clockwise in Fig. 13(b) and counterclockwise in Fig. 13(c). The waveforms at the nodes CW2, CW3, CW4, CW5, CCW2, CCW3, CCW4, and CCW5 in Fig. 8 were recorded. Since the image was focused on the area of the three inner circles, the MLE outputs of the fourth and fifth circles were kept at logic one. As can be seen in Fig. 13(b) [Fig. 13(c)], when the image was rotated clockwise (counterclockwise), CCW2 and CCW3 (CW2 and CW3) was kept at logic one and logic zero appear at CW2 and CW3 (CCW2 and CCW3). Thus, the direction of rotation was correctly detected.

Although the angular velocity was tuned to maximize R to 100%, CW2 and CW3 in Fig. 13(b), as well as CCW2 and CCW3 in Fig. 13(c), were not always at logic zero in each clock cycle. R measured with $N = 80$ was 50% and 66% for CW2 and CW3 in Fig. 13(b) and 52% and 70% for CCW2 and CCW3 in Fig. 13(c). The lowered R is caused by the misalignment effect described in Section II-D. As discussed in Section II-D, the maximum R decreases as r_n increases. Since the radius r of the third circle is larger than that of the second circle, while r_s is the same for both circles, the number of times for which MLE outputs logic zero at the second circle was less than that for which MLE outputs logic zero at the third circle, as can be seen in Fig. 13(b) and (c).

Fig. 14(d) plots the measured values of R versus angular velocity at CCW3 for the four patterns of Figs. 13(a) and 14(a)–(c). For the pattern in Fig. 14(a), θ_{ep} are 11.25° and 22.5°. For the pattern in Fig. 14(b), θ_{ep} for each edge are 0°, 5.125°, 11.25°, and 16.375°. The test image was rotated counterclockwise and the output at CCW3 was recorded to calculate R. The clock rate was 8 Hz, so the theoretical ω at which R was 100% was 2 π/s. As can be seen in Fig. 14(d), all four curves had a maximum R

at an angular velocity equal to 2 π/s. However, due to the imperfection of alignment, R did not reach 100% at that angular velocity. The imperfect alignment also degraded the angular velocity selectivity. According to the analysis in Section II-C, the theoretical angular velocities at which R goes to 0 are 1 and 3 π/s for the pattern in Fig. 13(a), 1.5 and 2.5 π/s for the pattern in Fig. 14(a), and 1.75 and 2.25 π/s for the pattern in Fig. 14(b). The pattern in Fig. 14(c) has many edges but the number and positions of the edges are too complicated to be analyzed. However, the maximum R at every ω is determined for the pattern in Fig. 14(c) since a equals two for the third circles. Thus, for this pattern, the theoretical values of angular velocity at which R is 0 should be greater than 1 π/s and less than 3 π/s, according to the analysis in Section II-C with $a = 2$. The measured angular velocities at which R goes to 0 were 1 and 3.2 π/s for the pattern in Fig. 13(a), 1.3 and 2.7 π/s for the pattern in Fig. 14(a), 1.5 and 2.4 π/s for the pattern in Fig. 14(b), and 1.2 and 2.7 π/s for the pattern in Fig. 14(c). Although the angular velocities at which R goes to 0 were disturbed by the misalignment effect, the effect of θ_{ep} on the angular velocity selectivity were consistent with the analysis in Section II. The angular velocity selectivity for the pattern in Fig. 14(b) is the best while the angular velocity selectivity for the pattern in Fig. 13(a) is the worst.

Fig. 15 presents the angular velocity selectivity at different clock rates. The angular velocity with maximum R can be controlled by the clock rate. The pattern in Fig. 13(a) was rotated counterclockwise and CCW3 was recorded to compute R. The CW3 was kept at logic one and was therefore not shown in Fig. 15. The clock rate was set to 0.01, 0.1, 1, 10, and 160 Hz. The angular velocities with maximum R were correctly the theoretical values, 0.0025, 0.025, 0.25, 2.5, and 40 π/s, respectively. The imperfection of the alignment prevented R from being 100%. As shown in Fig. 15, the angular velocity selectivity was verified at the clock rate that changed through four orders of magnitude from 0.01 to 160 Hz. Furthermore, the delay time can be as large as 100 s, which is impossible to be realized in a conventional RC circuit in integrated circuits technology.

On the other hand, if the image is rotated with a constant angular velocity, this rotation sensor can be used to measure the angular velocity by sweeping the clock rate and checking the occurrence of the maximum R, as shown in Fig. 16. The pattern in Fig. 13(a) was rotated counterclockwise and CCW3 was recorded. The CW3 was kept at logic one and was therefore
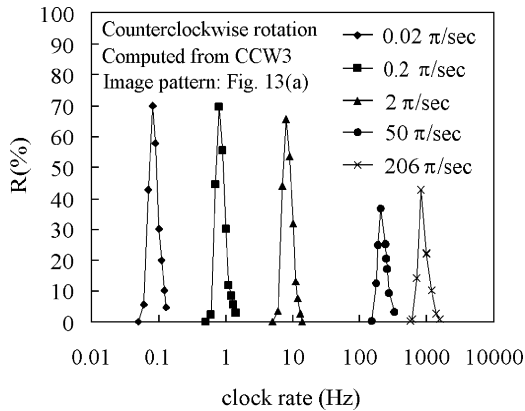
Fig. 16. Relationship between R and clock rate at angular velocities of 0.02, 0.2, 2, 50, and 206 pi/s. Clock rates when R is maximum at are 0.08, 0.8, 8, 200, and 824 Hz.
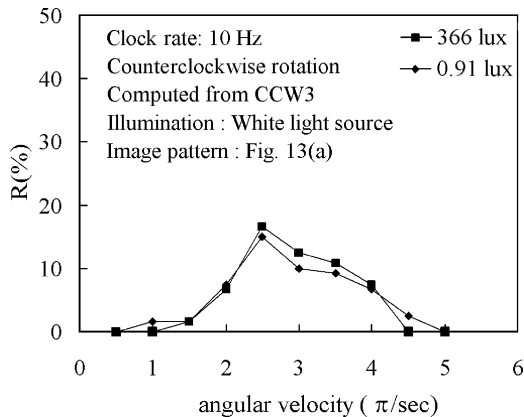

Fig. 17. Angular velocity selectivity under an illumination of 0.91 and 366 lux at a wavelength of 550 nm.

not shown in Fig. 16. The angular velocity of the rotating image was set to 0.02, 0.2, 2, 50, and 206 π/s. The clock rates that maximize R were correctly the theoretical values, 0.08, 0.8, 8, 200, and 824 Hz, respectively. The misalignment caused R to be less than 100%. The detectable range of angular velocity was at least four orders of magnitude, as shown in Fig. 16. The upper limit comes from the limited angular velocity of the motor in the measurement equipment. The lowest available clock rate of the clock signal generator imposes the lower limit on the detectable range.

Fig. 17 plots the angular velocity selectivity at the illumination of 0.91 and 366 lux at a wavelength of 550 nm. The pattern in Fig. 13(a) with a contrast of 80% was used. The image was rotated counterclockwise and CCW3 was recorded. The light source was a white light source. The clock rate was set to 10 Hz. Fig. 17 indicates that the angular velocity selectivity is only slightly degraded by the low illumination. The power dissipation at the illumination of 366 lux is 95 mW.

V. CONCLUSION

A CMOS focal-plane rotation sensor, which uses a retinal processing circuit and a correlation-based algorithm, is implemented and analyzed. The proposed rotation sensor has a polar structure and is selective to the angular velocity and direction

(clockwise and counterclockwise) of rotating images. The selected angular velocity is controlled by the period of a clock signal. The relationship between R and ω is derived to describe the angular velocity selectivity. The maximum R is 100% when the image is rotated by $\omega = \theta_s/T$. R is decreased if the angular velocity deviates from θ_s/T.

More than one pixel is placed between two correlated pixels, 45° apart, to enhance the angular velocity selectivity. The structure with more than one pixel between two correlated pixels is analyzed. The angular velocity at which R is decreased to zero is given by $\theta_s/T \pm \theta_s/aT$. Thus, the angular velocity selectivity is enhanced by increasing a.

If the incident image has multiple edges, then the angular velocity selectivity is related to both the number and positions of the edges and the value of R is confined in a range described by a set of inequalities. The upper bound of the range is reached if θ_{ep} are the same for every edge. The lower bound of the range is reached when θ_{ep} for every edge are equally distributed between 0 and θ_s/a.

An experimental rotation sensor chip was fabricated using the 0.6-CMOS process. The rotation sensor is comprised 104 pixels, which form five concentric circles. The numbers of pixels in the circles are 8, 16, 16, 32, and 32 in order from the center. The area of a single pixel is 91×84 μm^2, with a fill factor of 20%. The chip area is 1812×1825 μm^2. The dc power consumption was 10 mW at 5 V in the dark while that at the illumination of 366 lux is 95 mW. The experimental results concerning the fabricated chip verified that both the clockwise and the counterclockwise directions could be correctly detected. The angular velocity selectivity was also verified at a clock rate from 0.01 to 160 Hz. The proposed rotation sensor can be used to detect the angular velocity ranging from 2×10^{-2} to 206 π/s by sweeping the clock rate. The optical dynamic range at a contrast of 80% was 52 dB from 0.91 to 366 lux. It is found from the experimental results that the angular velocity selectivity is degraded by the misalignment effect. A practical method to solve this problem is to read out the sensed image and find the center of the rotating image. Then, precise motors can be used to adjust the position of the chip and align the center of the rotating image to the center of the circle of the pixels so that the error caused by misalignment effect can be reduced.
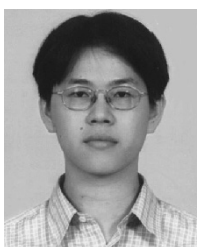
REFERENCES

[1] E. R. Fossum, "Architectures for focal-plane image processing," *Opt. Eng.*, vol. 28, no. 8, pp. 866–871, 1989.
[2] T. Delbruck, "Silicon retina with correlation-based velocity-tuned pixels," *IEEE Trans. Neural Networks*, vol. 4, pp. 529–541, May 1993.
[3] J. Tanner and C. A. Mead, "Correlation Optical Motion Detector," U.S. patent 4 631 400, Dec. 23, 1986.
[4] S. C. Liu, "A neuromorphic aVLSI model of global motion processing in the fly," *IEEE Trans. Circuits Syst. II*, vol. 47, pp. 1458–1467, Dec. 2000.
[5] R. C. Meitzler, K. Strohbehn, and A. G. Andreou, "A silicon retina for 2-D position and motion computation," in *Proc. 1995 IEEE Int. Symp. Circuits and Systems*, vol. 3, June 1995, pp. 2096–2099.

[6] A. G. Andreou, K. Strohbehn, and R. E. Jenkins, "Silicon retina for motion computation," in *Proc. 1991 IEEE Int. Symp. Circuits and Systems*, Singapore, June 1991, pp. 1373–1376.

[7] H. C. Jiang and C. Y. Wu, "A 2-D velocity- and direction-selective sensor with BJT-based silicon retina and temporal zero-crossing detector," *IEEE J. Solid-State Circuits*, vol. 34, pp. 241–247, Feb. 1999.

[8] C. Y. Wu and K. H. Huang, "A CMOS focal-plane motion sensor with BJT-based retinal smoothing network and modified correlation-based algorithm," *IEEE Sensors J.*, vol. 2, pp. 549–558, Dec. 2002.

[9] B. Hassenstein and W. Reichardt, "Systemtheoretische analyze der zeit-, reihenfolgen- und vorzeichenauswerttung bei der bewegungsperzeption des Russelkafers Chlorophanus," *Z. Naturforsch*, vol. 11b, pp. 513–524, 1956.

[10] C. Y. Wu and C. F. Chiu, "A new structure of 2-D silicon retina," *IEEE J. Solid-State Circuits*, vol. 30, pp. 890–897, Aug. 1995.

[11] C. Y. Wu and H. C. Jiang, "An improved BJT-based silicon retina with tunable image smoothing capability," *IEEE Trans. VLSI Syst.*, vol. 7, pp. 241–248, June 1999.

[12] Z. Wang and W. Guggenbuhl, "Novel CMOS current Schmitt trigger," *Electron Lett.*, vol. 24, no. 24, pp. 1514–1516, Nov. 1988.

Li-Ju Lin (S'00) was born in Taiwan, R.O.C., in 1976. She received the B.S. degree in electronics engineering from the National Chiao Tung University (NCTU), Hsinchu, Taiwan, in 1998. She is currently pursuing the Ph.D. degree at the Institute of Electronics, NCTU.

Her major research interests include silicon retina chip design and corresponding applications and cellular neural/nonlinear network.

Chung-Yu Wu (S'76–M'76–SM'96–F'98) was born in 1950. He received the M.S. and Ph.D. degrees from the Department of Electronics Engineering, National Chiao-Tung University (NCTU), Hsinchu, Taiwan, R.O.C., in 1976 and 1980, respectively.

Since 1980, he has served as a Consultant in the high-tech industry and research organizations and has built up strong research collaborations with high-tech industries. From 1980 to 1983, he was an Associate Professor at NCTU. From 1984 to 1986, he was a Visiting Associate Professor in the Department of Electrical Engineering, Portland State University, Portland, OR. Since 1987, he has been a Professor at NCTU. From 1991 to 1995, he was rotated to serve as the Director of the Division of Engineering and Applied Science on the National Science Council, Taiwan. From 1996 to 1998, he was honored as the Centennial Honorary Chair Professor, NCTU. In addition, he conducted postdoctoral research at UC Berkeley in summer of 2002. He has published more than 250 technical papers in international journals and conferences. He also holds 19 patents, including nine U.S. patents. His research interests are nanoelectronics and VLSI, including circuits and systems in low-power/low-voltage mixed-signal design, and systems, biochips, neural vision sensors, RF circuits, and CAD analysis.

Dr. Wu is a member of Eta Kappa Nu and Phi Tau Phi Honorary Scholastic Societies. He was a recipient of the IEEE Fellow Award in 1998 and the Third Millennium Medal in 2000. In Taiwan, he received numerous research awards from the Ministry of Education, National Science Council, and professional foundations.

Kuan-Hsun Huang (M'00) was born in Taiwan, R.O.C., in 1975. He received the B.S. and Ph.D. degrees in electronics engineering from the National Chiao Tung University, Hsinchu, Taiwan, in 1998 and 2003, respectively.

In 2003, he joined Faraday Technology Corporation. Since then, he has been engaged in the mixed-signal integrated circuit design.